nature chemistry

ARTICLES

https://doi.org/10.1038/s41557-021-00644-y

Check for updates

Reagentless biomolecular analysis using a molecular pendulum

Jagotamoy Das[1,5], Surath Gomis[2,5], Jenise B. Chen[3], Hanie Yousefi[1], Sharif Ahmed[1], Alam Mahmud[2], Wendi Zhou[2], Edward H. Sargent[2]✉ and Shana O. Kelley[1,3,4]✉

The development of reagentless sensors that can detect molecular analytes in biological fluids could enable a broad range of applications in personalized health monitoring. However, only a limited set of molecular inputs can currently be detected using reagentless sensors. Here, we report a sensing mechanism that is compatible with the analysis of proteins that are important physiological markers of stress, allergy, cardiovascular health, inflammation and cancer. The sensing method is based on the motion of an inverted molecular pendulum that exhibits field-induced transport modulated by the presence of a bound analyte. We measure the sensor's electric field-mediated transport using the electron-transfer kinetics of an attached reporter molecule. Using time-resolved electrochemical measurements that enable unidirectional motion of our sensor, the presence of an analyte bound to our sensor complex can be tracked continuously in real time. We show that this sensing approach is compatible with making measurements in blood, saliva, urine, tears and sweat and that the sensors can collect data in situ in living animals.

Self-regenerating sensors that can dynamically and continuously detect biomolecular species in physiological systems remain an unmet need[1,2]. The ability to monitor protein biomarkers in vivo would provide a powerful tool for disease monitoring and treatment response[3–5]. A key requirement for this type of sensing application is a reagentless assay format where all required elements are incorporated into a self-contained sensor to allow for autonomous function.

The most widely used sensors for reagentless, dynamic physiological monitoring at the molecular level rely on intrinsically redox-active chemistry or pathways that can be monitored at an electrode surface[5–12]. Reagentless electrochemical sensors that are, instead, affinity-based and compatible with in vivo monitoring applications have been generated based on DNA aptamers and other DNA-based constructs that serve as recognition elements[13–18]. Aptamers that exhibit analyte-induced conformational switching can be used to transduce the presence of a variety of analytes by modulating the distance between an electrode and the redox indicator methylene blue[19–23]. Sensors featuring double-stranded DNA with a small recognition element displayed distal to the electrode surface have also enabled readout of a variety of antibodies and other proteins[24–27]. The sensors developed using this approach have addressed a variety of challenging problems, including in vivo sensing of small molecules and the detection of antibodies associated with infectious disease. However, existing affinity-based sensors are limited to recognition agents based on small molecules, peptide epitopes and small proteins, because diffusion of the sensor complex to the surface is relatively slow[28,29].

We hypothesized that, by designing sensors featuring field-mediated transport to the electrode surface, we could create constructs that could be used with any recognition agent of interest. A simple model was created to explore theoretically the feasibility of creating sensors based on this approach that informed the design of sensor constructs and choice of a redox indicator. Using a redox-active moiety that is electrically active at a potential compatible with the generation of a positive electrical field, we could simultaneously attract a negatively charged, DNA-based sensor to the electrode surface and measure electron-transfer dynamics. Potential-dependent modulation of DNA orientation on electrode surfaces has been observed in previous studies[30–32], so this material appeared appropriate for the potential-responsive linker of our sensor. The use of chronoamperometry, with its persistent step potential, provides an ideal means to read out the kinetic information that reports on whether a recognition element (that is, antibody) is present in a bound or unbound state. Using this approach, we demonstrate that a range of protein analytes can be detected using a reagentless format in a series of biological fluids and also in living animals. This approach provides a generalizable means to monitor a wide variety of analytes that are incompatible with previous approaches.

Results

Theoretical model of a molecular pendulum. We first investigated whether it would be possible to differentiate molecular complexes using a simple theoretical analysis exploring the motion of a tethered nanoscale sensor complex, modelled from first principles as an inverted molecular pendulum (MP). The pendulum rod approximates a rigid charged linker, while a circular pendulum bob represents the recognition element and analyte contribution. With this approach, we could monitor the time-dependent fall time of the MP under competing forces of hydrodynamic drag and electrostatic interactions contributed by components of the MP, all working against the driving force of an attractive electric field. Although, in the model, molecular-level physical intricacies are not taken into account, we envisioned that the rigid charged linker would be composed of DNA and the recognition element would be an analyte-specific antibody.

[1]Leslie Dan Faculty of Pharmacy, University of Toronto, Toronto, Ontario, Canada. [2]The Edward S. Rogers Sr. Department of Electrical and Computer Engineering, University of Toronto, Toronto, Ontario, Canada. [3]Department of Chemistry, University of Toronto, Toronto, Ontario, Canada. [4]Institute of Biomaterials and Biomedical Engineering, University of Toronto, Toronto, Ontario, Canada. [5]These authors contributed equally: Jagotamoy Das, Surath Gomis. ✉e-mail: ted.sargent@utoronto.ca; shana.kelley@utoronto.ca

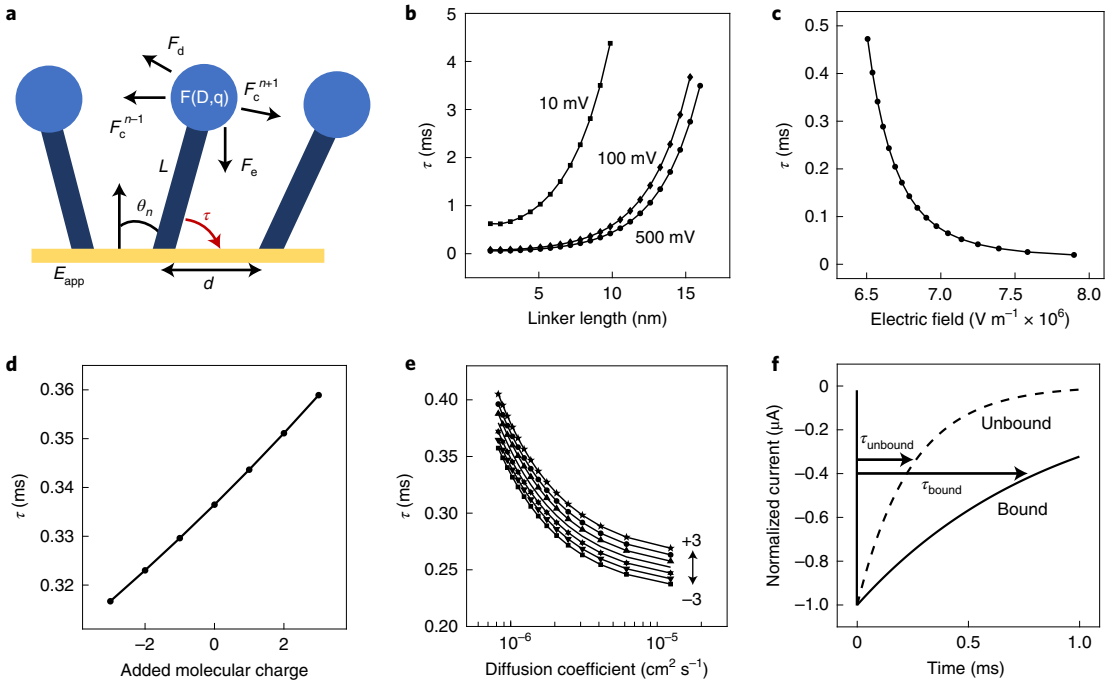

Fig. 1 | Modelling the dynamics of the MP tethered to an electrode surface. a, The model parameters. The dynamics of the MP were modelled by considering the drag force (F_d), the force exerted by the applied field (F_e) and electrostatic interactions between neighbouring MPs (F_c), and how they all vary according to the analyte that becomes incorporated into the 'bob'. The length of the linker (L), the distance between neighbouring MPs (d), the average angle of the MPs relative to the surface (θ), the molecular charge (q), the diffusion coefficient (D) and the applied electric field (E_{app}) were all varied to explore the MP dynamics. Under an applied positive potential, a negatively charged MP is attracted to the sensor surface. The transit time of the MP is reflected in the τ value determined by simulating the EOMs for a particular MP configuration through transit angle θ until it reaches the electrode. **b**, Dependence of τ on the length of a negatively charged linker. Linkers of ~10 nm appear optimal for microsecond MP transport. **c**, Dependence of τ on the magnitude of the applied electric field. As the average applied electric field increases, τ decreases as the MP is more strongly attracted towards the electrode surface. This is expected for a negatively charged MP accelerating through the field gradient of a positively applied potential. **d**, Dependence of τ on added molecular charge. Added molecular charge causes very small variations in τ. **e**, Dependence of τ on the diffusion coefficient. As the diffusion coefficient of the analyte is increased with decreasing molecular weight and size, τ decreases as the effect of F_d is reduced. Consideration of a charged analyte produces modulations in τ. **f**, The modelled current decay expected if the dynamics of the MP could be monitored using an electrochemically active label in the absence and presence of a molecular cargo 20 nm in size, and with an applied electrode potential of 500 mV. The current traces were drawn considering a characteristic time in the form of $I_0e^{-t/\tau}$. It is notable that the current response of field-induced MP transport is on the microsecond timescale.

As the negatively charged MP pivots down through the electric field (F_e) induced by a positive applied potential (E_{app}), it experiences a hydrodynamic drag force (F_d) and forces caused by Coulombic interactions (F_c) with neighbouring MPs spaced a distance (d) apart in a monolayer of MPs. These interactions modulate the time (τ) required for the MP to reach the electrode surface (Fig. 1a, Supplementary Figs. 1–6 and Supplementary Table 1). The τ of the MP configuration was determined by solving for its equations of motion (EOMs) (Methods, 'Model formulation') and it was elucidated that τ values induced by field-mediated transport would span the hundreds-of-microseconds regime with a strong applied potential.

We explored (Fig. 1b–e) the role of linker length, electric field strength, changes in molecular charge, as well as variations in cargo size and diffusion coefficient, and observed that all of these parameters modulated the τ values observed. With applied potential, the τ values approached the millisecond range due to the electrostatic interaction between the MP and electrode, and a range of linkers that provide high levels of charge in stronger fields exhibited smaller τ values approaching 20 μs. Variations in molecular charge produced changes in τ, but the MP is generally more sensitive to variations in size—and hence the diffusion coefficients—of the recognition element and analytes. We then used the model to simulate electrochemical current responses in the form $I_0e^{-t/\tau}$ to visualize a molecular size change of 20 nm (Fig. 1f). Pronounced changes to the current profiles were observed, indicating that microsecond changes in τ could be correlated to experimentally observable electrochemical currents with microampere resolution.

Experimental validations of the MP model. We next explored these phenomena experimentally (Fig. 2 and Supplementary Figs. 7–14). To experimentally monitor τ, it was crucial to choose a redox reporter compatible with an applied positive electrode potential, such that the electrochemical oxidation of the reporter would be concomitant with the field-mediated transport of the sensor to the electrode surface. We thus chose the reporter ferrocene, which is oxidized at ~+400 mV versus Ag/AgCl, to be attached to our MP. This led us to choose an electrode potential of +500 mV to enable field-mediated MP transport. MP transport brings the bound ferrocene to the electrode surface to oxidize, with the transport process being rate-limiting given ferrocene's fast electron-transfer kinetics[33]. The MPs used for initial experimental demonstration of the system featured a 24-base-pair DNA linker and an antibody specific for cardiac troponin I.

As our MP method relies on a positive potential step to facilitate MP movement, we chose chronoamperometry to measure the faradaic current from the redox reporter. For the MP in its unbound state, a τ value of ~100 μs was measured, whereas in the presence of added protein, the MP in its bound state exhibited a τ value of ~300 μs

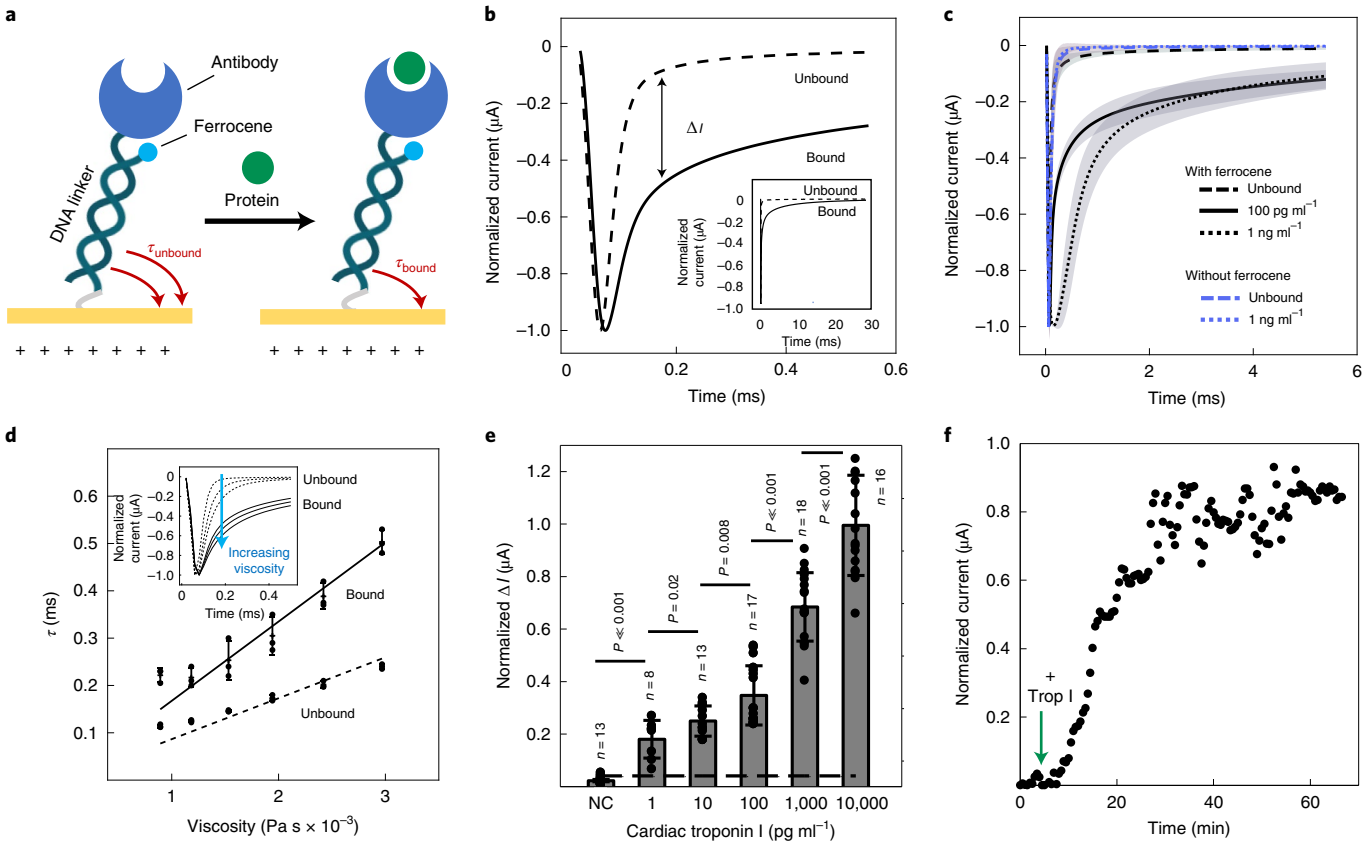

Fig. 2 | Modulation of MP dynamics by protein binding. a, A protein-binding MP was constructed using double-stranded DNA and an antibody specific for troponin I. A redox reporter, ferrocene, was incorporated into the DNA linker. This would be oxidized at an electrode potential compatible with the electric field required to transport the MP to the surface, a key consideration that enables MP transport measurement. **b**, Observation of binding-induced modulation of MP transport using chronoamperometry in the presence (solid line) and absence (dashed line) of troponin I (100 pg ml^{-1}). Inset: the full chronoamperometry traces collected with a potential step of +500 mV. Both τ and ΔI can be used to monitor the response of the system, as ΔI is measured beyond the peak at 200 μs, and τ is measured at 1/e peak current. **c**, Evaluation of capacitive versus faradaic currents for MP sensors. When MPs lacking ferrocene were tested, both unbound and troponin-bound MPs produce small capactive currents (Supplementary Fig. 8 shows the MP response for a shorter time window). When comparing the same unbound and troponin-bound MPs with ferrocene attached, the faradaic current responses are present, demonstrating that modulations of τ reflect oxidation of the ferrocene reporter. Standard deviations are shown as grey shaded lines, with $n = 5$ for each trace. **d**, Comparison of observed and calculated τ values for bound and unbound MPs in solutions with various viscosities. By changing the viscosity of the medium using increasingly higher glycerol concentrations, the MP encounters higher drag force during transit and τ increases. The computational results (line plot) match the decay characteristics of the experimental MP time response (data points) for the bound and unbound states. Error bars represent standard deviations. Inset: current traces of bound and unbound MPs, where increasing viscosity produces larger τ values and thus slower current responses. **e**, Concentration-dependent signal change for cardiac troponin I in buffered solution suggests that the bound state ΔI is distinguishable down to 1 pg ml^{-1}. Data from unbound MPs have been subtracted and are shown as a control line of three standard deviations, used as the cutoff values for the limit of detection. The negative control (NC) uses anti-troponin MPs presented with 1 ng ml^{-1} of RANTES protein. Error bars represent standard deviations, currents were normalized to the highest concentration and the absolute value is shown. Centres of error bars represent mean values. Currents from each concentration are statistically significant from one another ($P < 0.05$; two-sided, two-sample t-tests). **f**, Time-dependent current modulation for MPs in the presence of troponin I demonstrates the change in measurable current and equilibration within ~20 min. Troponin I was injected into solution at $t = 7$ min and a chronoamperometric measurement was taken every 30 s. The current magnitude is shown as an absolute value.

(Fig. 2b). The values for τ are measured at 1/e the peak current value, with a current difference (ΔI) at 200 μs between the bound and unbound state providing a convenient means to measure the changes in field-mediated transport. It is noteworthy that cyclic voltammetry and square-wave voltammetry scans revealed very low levels of current (Supplementary Fig. 7), probably because of the absence of a strong applied potential throughout the measurement and the distance between the ferrocene reported and the electrode surface.

To assess the contribution of capacitive versus faradaic currents to the analyte-modulated signal, we tested a control MP lacking the ferrocene redox reporter. Fast decays for these control assemblies were observed with and without analyte, indicating that the longer decay monitored in the ΔI measurements at 200 μs reflected faradaic current generated by the ferrocene label (Fig. 2c and Supplementary Fig. 8). It is noteworthy that the kinetics observed here are much faster than those observed for methylene blue-based sensors, probably because of the surface charge being negative at the reduction potential employed in that system and the electrostatic repulsion of the DNA[34–37]. Additional experiments (Supplementary Figs. 9 and 10) exploring alternative potential step patterns confirmed that the application of a strong positive potential was critical to enable the measurement of field-induced MP transport.

To explore the variation in transport times of the tethered MP, we varied the drag force on the tethered complex by altering the solution viscosity with added glycerol. Calculation of the τ values as a function of the drag force investigated experimentally indicated

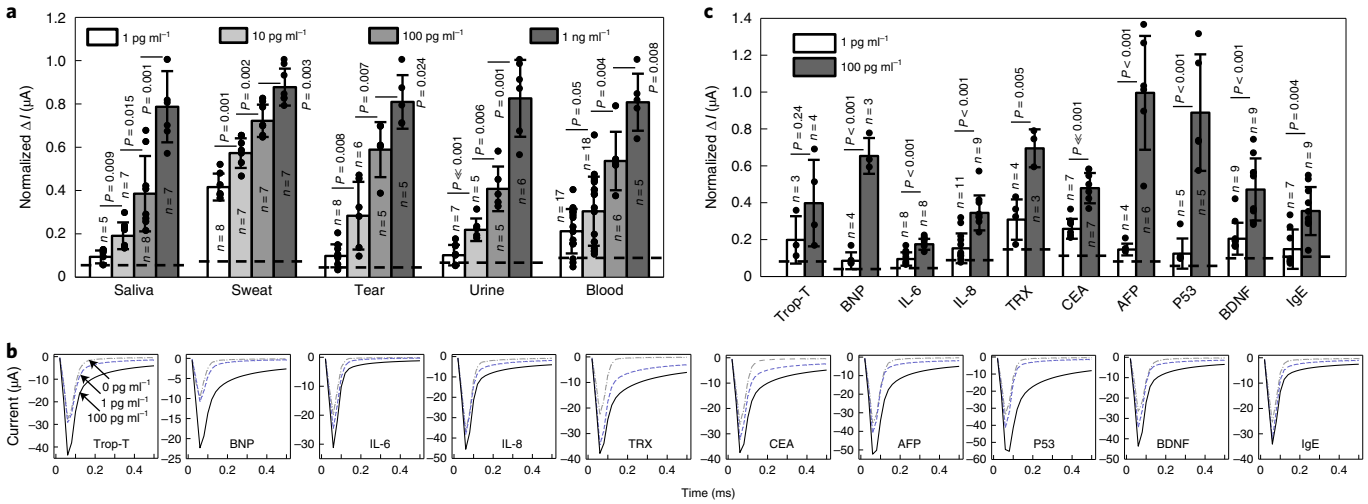

Fig. 3 | Panel of proteins and biofluids that can be monitored using MPs. a, Detection of cardiac troponin I in different biofluids including saliva, sweat, tears, urine and blood. Data from unbound MPs have been subtracted and dashed lines represent cutoff values for the limit of detection, represented as three standard deviations of values from unbound MPs incubated with only the corresponding biofluid. Error bars represent standard deviations, and centres of error bars represent mean values. Statistically significant currents between concentrations are shown ($P < 0.05$; two-sided, two-sample *t*-tests). **b**, Testing of a panel of MPs specific for cardiac, inflammation, stress and cancer markers. Significant changes in response to higher concentrations of biomarkers were observed compared to background. Raw current traces are shown. Trop-T, troponin T; BNP, brain-derived neurotrophic factor; IL-6, interleukin-6; TRX, thioredoxin; CEA, carcino embryonic antigen; AFP, alpha 1 fetoprotein; P53, P53 protein; BDNF, brain-derived neurotrophic factor; IgE, immunoglobulin-E. **c**, Concentration-dependent responses for each protein tested. Changes in the current response curves were distinguishable for unbound and bound MPs specific to each protein tested. Data from unbound MPs have been subtracted, and dashed lines represent cutoff values for the limit of detection, represented as three standard deviations of values from unbound MPs. Error bars represent standard deviations, and centres of error bars represent mean values. Statistically significant currents between concentrations are shown ($P < 0.05$; two-sided, two-sample *t*-tests).

good agreement with our model (Fig. 2d), suggesting that we can calibrate our model across different fluid matrices. The addition of a secondary antibody to the MP complex was shown to increase transport time further (Supplementary Fig. 11), consistent with the original modelling effort. Studies exploring the density of surface coverage (Supplementary Figs. 12 and 13), which would modulate field-induced transport by introducing additional electrostatic and steric interactions, also indicated that these parameters play a role in modulating the kinetics of MP transport to the electrode surface.

Concentration-dependent sensor response to target proteins. We also observed increased τ values and resultant changes in current for the bound state of the MP complex as a function of analyte (cardiac troponin I) concentration (Fig. 2e and Supplementary Fig. 14). The dynamic range of our sensor is observed in the linear portion of our concentration curve, from ~100 pg ml^{-1} to 10 ng ml^{-1}. However, at concentrations of troponin I as low as 1 pg ml^{-1} (~40 fM), statistically significant changes in current were observed. The increasing current differences at these low protein concentrations may reflect the ability of this sensing system to detect low levels of sensor occupancy (Supplementary Fig. 14) as well as the effects of locally high sensor concentrations at the electrode surface[38,39]. To explore the kinetics of analyte binding to an MP, we collected current transients as a function of incubation time and determined that changes in the current could be observed within 10 min (Fig. 2f). In the presence of non-target proteins or a sensor where the antibody was replaced by bovine serum albumin (BSA), large current modulations were not observed.

Detection in different biological fluids. To challenge the specificity of the MP for the target protein troponin I, we tested whether the concentration-dependent current changes would be retained in biological fluids including saliva, urine, tear fluid, blood and sweat (Fig. 3a and Supplementary Fig. 15). Small fluctuations in the current transients, tabulated as ΔI values, were observed as a function of the type of fluid present, and statistically significant changes in current were observed with 1 pg ml^{-1} of troponin I for all sample types tested, except in blood where there was slightly more noise. Small variations in the magnitude of the effect were observed with the different sample types, probably due to changes in ionic strength or viscosity caused by the composition of the different fluids. However, the retention of performance in these different fluids over a range of statistically significant concentrations is a key feature of this system that reflects the dynamic measurements that are the foundation of our approach.

Analysis of the protein biomarker panel. A panel of proteins were tested to explore whether the binding-induced modulation of MPs was a general effect (Fig. 3b,c and Supplementary Table 2). We tested a panel of 10 different proteins with varying charges, sizes and molecular weights, using MPs that featured antibodies specific for each protein. Chronoamperometry was used to monitor the change in τ values in the presence of two different concentrations of each protein, and each factor could be reproducibly monitored. Smaller proteins (for example, interleukin-6 (IL-6)) produced more subtle changes to the current transients for the corresponding MPs compared to larger proteins, as expected using our MP theoretical model. Overall, all proteins were detectable using MPs, with significant currents above unbound sensors (represented by control lines in Fig. 3c). These results demonstrate that MP transport behaviour, when resolved using kinetic measurements, provides a universal reporter on biomolecular complexation status.

Animal model and in vivo analysis of a protein biomarker. We then turned to exploring whether our MP constructs could be used for dynamic, continuous monitoring in living systems (Fig. 4 and Supplementary Figs. 16–22). We first tested the reversibility of the signals observed for troponin I-specific MPs. We observed

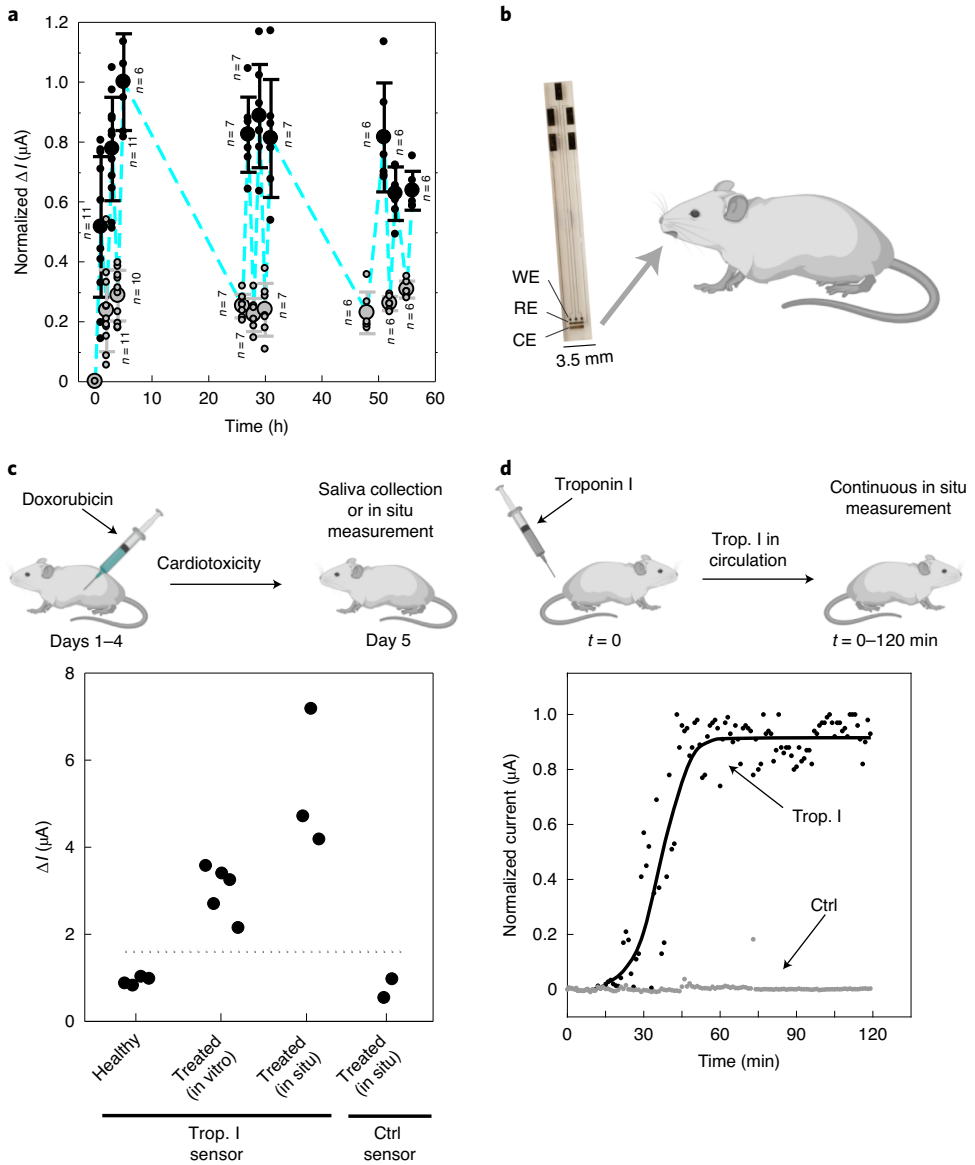

Fig. 4 | MP-based monitoring of a cardiac marker in living animals. a, Short-term cycling of MP signals. Black circles indicate the signal change of the MP when it is incubated with target protein (10 ng ml^{-1}) for 50 min, and the grey circles represent the signal change when the MP is incubated with either buffered solution or a non-target protein (10 ng ml^{-1}) for at least 50 min, demonstrating antibody–protein dissociation with minimal sensor current decay, and hence reusability of the sensor. Error bars represent standard deviations, and centres of error bars represent mean values. **b**, The MP sensor used for animal studies. Small MP sensors were fabricated with gold contacts on a glass substrate, where the active electrode area can be placed in the anaesthetized animal's mouth to be submerged in saliva. These sensors are elongated to clamp interconnects for the potentiostat. WE, working electrode; RE, reference electrode; CE, counter electrode. **c**, Measurement of troponin I in saliva both ex situ and in situ using MPs. To induce cardiac dysfunction, mice were treated with doxorubicin for four days and saliva samples were collected at day 5 for ex situ/in vitro measurements, or single point measurements were collected within the mouth. Each data point represents a measurement obtained with different mice. **d**, In situ continuous monitoring of cardiac troponin I in a murine model. Mice were injected with cardiac troponin I 45 min before data acquisition, and the MP signal change was monitored continuously after 10 min of sensor equilibration with MPs featuring a troponin I antibody or BSA (Ctrl). The data shown are representative of signal changes observed in independent replicates. Current magnitude is shown.

that the current changes triggered by the presence of the protein disappeared within 1 h when the protein was no longer present (Fig. 4a). Multiple cycles of protein and blank incubation indicated that the MPs were stable on the timescale of hours, and longer incubations between cycles showed that the system was stable over days. MPs could also be stored in biological fluids like saliva for multiple weeks and remained stable (Supplementary Fig. 19). Although other studies have observed degradation of sensor performance over timescales ranging from hours to days, the response of the MP sensors appeared quite stable, probably due to the short sampling times (Supplementary Figs. 20 and 21) and the use of time-resolved measurements in the analysis that would not be sensitive to small losses in surface coverage[40].

We pursued the measurement of troponin I in living animals by testing two models. The first model was one that uses drug-induced cardiotoxicity to induce cardiac failure in mice[41], which is known to induce the release of troponin into the blood stream and saliva. Mice were treated for four days with doxorubicin, and on the

fifth day the animals were tested in situ using MP-functionalized electrodes, designed to partially fit within the mouse mouth such that the electrodes were constantly wetted by saliva (Fig. 4b and Supplementary Figs. 23–25). Elevated current levels were measured for a treated cohort of mice relative to untreated mice. Mice were also tested with control MPs that did not possess a specific antibody, and baseline levels of current were detected (Fig. 4c). The second model tested involved direct injection of troponin I into mice and continuous monitoring using a troponin I or control MP sensor in the oral cavity of a mouse (Fig. 4d). Within 1 h after injection of the protein, increases in the differential currents were measured for the troponin I sensors, while the control sensor current levels remained at baseline.

Discussion

The sensors reported here enable the in vivo monitoring of physiologically relevant protein biomarkers in living animals. Although the composition of the MP sensors is similar to other reagentless systems reported previously[13–27], their operation is distinct in several respects. The MP system was designed to take advantage of active, field-mediated transport of the sensor to the electrode surface so that the electron-transfer kinetics could be tracked on a timescale consistent with short, chronoamperometry-based analyses. Existing electrochemical sensors based on aptamers or DNA-functionalized constructs, although widely utilized in a number of sensing applications, use redox-active labels that produce a negative surface charge that prevents rapid electron transfer because of repulsive electrostatic interactions. This prevents the use of large recognition agents including antibodies (Supplementary Fig. 26). It is also noteworthy that potential-based transport has been used to monitor protein–protein interactions at a gold surface[42–44], but the fluorescence-based analysis used to monitor this phenomenon is not amenable to the in situ monitoring applications showcased here.

These results indicate that sensors based on MPs provide a general approach for the development of implantable sensors that can be used to monitor physiologically relevant proteins directly in biofluids. Given recent advances in the development of wearable monitoring devices[45–47], this protein sensing concept may find broad applicability. Other recent advances in the development of reagentless protein sensors provide additional options for designing autonomous, self-regenerating sensors[13]. Furthermore, with the simple design of MP sensors and compatibility with a wide range of targets including nucleic acids, antibodies and microorganisms, the approach may also find utility in the development of clinical diagnostics. The development of versatile sensors that can track molecular analytes in biological fluids remains an unmet need now fulfilled by the performance exhibited by the MP approach.

Online content

Any methods, additional references, Nature Research reporting summaries, source data, extended data, supplementary information, acknowledgements, peer review information; details of author contributions and competing interests; and statements of data and code availability are available at https://doi.org/10.1038/s41557-021-00644-y.

Received: 15 April 2020; Accepted: 22 January 2021;
Published online: 08 March 2021

References

1. Kim, J., Campbell, A. S., de Ávila, B. E. F. & Wang, J. Wearable biosensors for healthcare monitoring. *Nat. Biotechnol.* **37**, 389–406 (2019).
2. Bandodkar, A. J., Jeang, W. J., Ghaffari, R. & Rogers, J. A. Wearable sensors for biochemical sweat analysis. *Annu. Rev. Anal. Chem.* **12**, 1–22 (2019).
3. Giljohann, D. A. & Mirkin, C. A. Drivers of biodiagnostic development. *Nature* **462**, 461–464 (2009).
4. Gaster, R. S. et al. Matrix-insensitive protein assays push the limits of biosensors in medicine. *Nat. Med.* **15**, 1327–1332 (2009).
5. Rong, G., Corrie, S. R. & Clark, H. A. In vivo biosensing: progress and perspectives. *ACS Sens.* **2**, 327–338 (2017).
6. Gao, W. et al. Fully integrated wearable sensor arrays for multiplexed in situ perspiration analysis. *Nature* **529**, 509–514 (2016).
7. Wassum, K. M. et al. Transient extracellular glutamate events in the basolateral amygdala track reward-seeking actions. *J. Neurosci.* **32**, 2734–2746 (2012).
8. Sarter, M. & Kim, Y. Interpreting chemical neurotransmission in vivo: techniques, time scales and theories. *ACS Chem. Neurosci.* **6**, 8–10 (2015).
9. Lipani, L. et al. Non-invasive, transdermal, path-selective and specific glucose monitoring via a graphene-based platform. *Nat. Nanotechnol.* **13**, 504–511 (2018).
10. Lee, H. et al. A graphene-based electrochemical device with thermoresponsive microneedles for diabetes monitoring and therapy. *Nat. Nanotechnol.* **11**, 566–572 (2016).
11. Bindra, D. S. et al. Design and in vitro studies of a needle-type glucose sensor for subcutaneous monitoring. *Anal. Chem.* **63**, 1692–1696 (1991).
12. Koh, A. et al. A soft, wearable microfluidic device for the capture, storage and colorimetric sensing of sweat. *Sci. Transl. Med.* **8**, 366ra165 (2016).
13. Kang, D. et al. New architecture for reagentless, protein-based electrochemical biosensors. *J. Am. Chem. Soc.* **139**, 12113–12116 (2017).
14. Arroyo-Currás, N. et al. Real-time measurement of small molecules directly in awake, ambulatory animals. *Proc. Natl Acad. Sci. USA* **114**, 645–650 (2017).
15. Ferguson, B. S. et al. Real-time, aptamer-based tracking of circulating therapeutic agents in living animals. *Sci. Transl. Med.* **5**, 213ra165 (2013).
16. Mage, P. L. et al. Closed-loop control of circulating drug levels in live animals. *Nat. Biomed. Eng.* **1**, 0070 (2017).
17. Somasundaram, S. & Easley, C. J. A nucleic acid nanostructure built through on-electrode ligation for electrochemical detection of a broad range of analytes. *J. Am. Chem. Soc.* **141**, 11721–11726 (2019).
18. Nakatsuka, N. et al. Aptamer–field-effect transistors overcome Debye length limitations for small-molecule sensing. *Science* **362**, 319–324 (2018).
19. White, R. J. & Plaxco, K. W. Exploiting binding-induced changes in probe flexibility for the optimization of electrochemical biosensors. *Anal. Chem.* **82**, 73–76 (2010).
20. White, R. J., Phares, N., Lubin, A. A., Xiao, Y. & Plaxco, K. W. Optimization of electrochemical aptamer-based sensors via optimization of probe packing density and surface chemistry. *Langmuir* **24**, 10513–10518 (2008).
21. Ferapontova, E. E. & Gothelf, K. V. Optimization of the electrochemical RNA-aptamer based biosensor for theophylline by using a methylene blue redox label. *Electroanalysis* **21**, 1261–1266 (2009).
22. Xiao, Y., Uzawa, T., White, R. J., DeMartini, D. & Plaxco, K. W. On the signaling of electrochemical aptamer-based sensors: collision- and folding-based mechanisms. *Electroanalysis* **21**, 1267–1271 (2009).
23. Pellitero, M. A., Shaver, A. & Arroyo-Currás, N. Critical review—approaches for the electrochemical interrogation of DNA-based sensors: a critical review. *J. Electrochem. Soc.* **167**, 037529 (2020).
24. White, R. J. et al. Wash-free, electrochemical platform for the quantitative, multiplexed detection of specific antibodies. *Anal. Chem.* **84**, 1098–1103 (2012).
25. Plaxco, K. W., Cash, K. J. & Ricci, F. An electrochemical sensor for the detection of protein-small molecule interactions directly in serum and other complex matrices. *J. Am. Chem. Soc.* **131**, 6955–6957 (2009).
26. Parolo, C. et al. E-DNA scaffold sensors and the reagentless, single-step, measurement of HIV-diagnostic antibodies in human serum. *Microsyst. Nanoeng.* **6**, 4–11 (2020).
27. Ogden, N. E., Kurnik, M., Parolo, C. & Plaxco, K. W. An electrochemical scaffold sensor for rapid syphilis diagnosis. *Analyst* **144**, 5277–5283 (2019).
28. Kang, D. et al. Expanding the scope of protein-detecting electrochemical DNA 'scaffold' sensors. *ACS Sens.* **3**, 1271–1275 (2018).
29. Huang, K. C. & White, R. J. Random walk on a leash: a simple single-molecule diffusion model for surface-tethered redox molecules with flexible linkers. *J. Am. Chem. Soc.* **135**, 12808–12817 (2013).
30. Kelley, S. O. et al. Orienting DNA helices on gold using applied electric fields. *Langmuir* **14**, 6781–6784 (1998).
31. Erdmann, M., David, R., Fornof, A. & Gaub, H. E. Electrically controlled DNA adhesion. *Nat. Nanotechnol.* **5**, 154–159 (2010).
32. Langer, A., Kaiser, W., Svejda, M., Schwertler, P. & Rant, U. Molecular dynamics of DNA–protein conjugates on electrified surfaces: solutions to the drift-diffusion equation. *J. Phys. Chem. B* **118**, 597–607 (2014).
33. Dauphin-Ducharme, P. et al. Simulation-based approach to determining electron transfer rates using square-wave voltammetry. *Langmuir* **33**, 4407–4413 (2017).
34. Uzawa, T., Cheng, R. R., White, R. J., Makarov, D. E. & Plaxco, K. W. A mechanistic study of electron transfer from the distal termini of electrode-bound, single-stranded DNAs. *J. Am. Chem. Soc.* **132**, 16120–16126 (2010).
35. Arroyo-Currás, N. et al. Subsecond-resolved molecular measurements in the living body using chronoamperometrically interrogated aptamer-based sensors. *ACS Sens.* **3**, 360–366 (2018).

36. Dauphin-Ducharme, P. et al. Chain dynamics limit electron transfer from electrode-bound, single-stranded oligonucleotides. *J. Phys. Chem. C* **122**, 21441–21448 (2018).
37. Santos-Cancel, M., Lazenby, R. A. & White, R. J. Rapid two-millisecond interrogation of electrochemical, aptamer-based sensor response using intermittent pulse amperometry. *ACS Sens.* **3**, 1203–1209 (2018).
38. Das, J. & Kelley, S. O. Tuning the bacterial detection sensitivity of nanostructured microelectrodes. *Anal. Chem.* **85**, 7333–7338 (2013).
39. Esteban Fernández De Ávila, B. et al. Determinants of the detection limit and specificity of surface-based biosensors. *Anal. Chem.* **85**, 6593–6597 (2013).
40. Shaver, A., Curtis, S. D. & Arroyo-Currás, N. Alkanethiol monolayer end groups affect the long-term operational stability and signaling of electrochemical, aptamer-based sensors in biological fluids. *ACS Appl. Mater. Interfaces* **12**, 11214–11223 (2020).
41. Herman, E. H. & Ferrans, V. J. Preclinical animal models of cardiac protection from anthracycline-induced cardiotoxicity. *Semin. Oncol.* **25**, 15–21 (1998).
42. Langer, A. et al. Protein analysis by time-resolved measurements with an electro-switchable DNA chip. *Nat. Commun.* **4**, 2099 (2013).
43. Rant, U. et al. Detection and size analysis of proteins with switchable DNA layers. *Nano Lett.* **9**, 1290–1295 (2009).
44. Knezevic, J. et al. Quantitation of affinity, avidity and binding kinetics of protein analytes with a dynamically switchable biosurface. *J. Am. Chem. Soc.* **134**, 15225–15228 (2012).
45. Yang, Y. et al. A laser-engraved wearable sensor for sensitive detection of uric acid and tyrosine in sweat. *Nat. Biotechnol.* **38**, 217–224 (2020).
46. Xu, S. et al. Soft microfluidic assemblies of sensors, circuits and radios for the skin. *Science* **344**, 70–74 (2014).
47. Wang, S. et al. Skin electronics from scalable fabrication of an intrinsically stretchable transistor array. *Nature* **555**, 83–88 (2018).

Methods

Model formulation. We sought to model our sensor from first principles as an inverted pendulum. The rod of the pendulum is a rigid linker, such as double-stranded DNA, and the bob of the pendulum is both the recognition element and analyte, such as an antibody and bound protein. We believed that a biomolecular analyte sensor could be created by sensing the changes in motion of the bound and unbound pendulum based on how its bob would fall against competing drag and electrostatic forces. We reasoned that these forces would have considerable effects at the microscale due to their size-dependent nature, and the best way to model such a system would be by using classical mechanics. Whereas most treatments of electrochemical systems strictly deal with the statistical mechanics of free ions, the sensing probes in our system are tethered linkers pivoting towards an electrode by drifting within an electric field. This led us to model the system's transport dynamics by considering the competing forces driving pendulum motion.

For this formulation, we concentrated the charge (q), mass (m) and size (R) of the system into the bob. The rigid rod then connects the bob to the electrode surface. This inverted pendulum, which we call our MP, is fixed at the origin of a two-dimensional plane and is allowed to pivot through all angles $-\frac{\pi}{2} \leq \theta \leq \frac{\pi}{2}$ about the vertical axis.

Next, we asserted that the most important external forces acting in the system would be the Lorentz force, which pulls or pushes the bob (contributed by the charged linker, recognition element and analyte), and the Stokes' drag, which acts against the rotational motion of the bob. In addition, Coulomb interactions between neighbouring MPs would be crucial to consider in a dense monolayer of sensors, and steric restrictions were accounted for by limiting the MP motion in the range of θ described previously.

We modelled the electric field generated in our bulk electrolyte using the Gouy–Chapman model assuming the MP monolayer does not interact with the static field formation. In solving for the EOMs for the system, we modelled three interacting MPs and forced periodic boundary conditions such that each MP interacted with its neighbouring MPs (this makes the system equivalent to a monolayer of MPs where we can choose a distance between each MP to modify monolayer density).

A 50 nm × 50 nm discretized space was generated with 0.01 nm × 0.01 nm square cells for our computational model. The Gouy–Chapman potential[48] was solved along the vertical axis, y, using the following equation:

$$\phi(y) = \frac{4kT}{ze}\operatorname{atanh}\left(\tanh\left(\frac{ze\phi_0}{4kT}\right)e^{-\kappa y}\right) \tag{1}$$

Here, z is the signed charge of the electrolyte, e is the electronic charge, ϕ_0 is the potential applied to the electrode, k_B is the Boltzmann constant and T is absolute temperature. The κ in the exponential decay term is equal to

$$\kappa = \left(\frac{2n^0 z^2 e^2}{\epsilon_r \epsilon_0 k_B T}\right)^{\frac{1}{2}} \tag{2}$$

Here, n^0 is the bulk number concentration of the electrolyte (per cubic metre), which can be found from molar concentration C_0 and Avogadro's number N_A through the relation $n^0 = 1{,}000 \times C^0 \times N_A$, while ε_0 is the permittivity of free space and ε_r is the relative permittivity of the electrolyte solution. The electric field is numerically solved by using the central difference method on $E = -\frac{d\phi}{dy}$ for our discretized system.

With the electric field established in our two-dimensional domain, we then derived the EOMs for the MP monolayer using the following forces:

$$\mathbf{F}_d = 6\pi\eta R\mathbf{v} \tag{3}$$

$$\mathbf{F}_e = q'\mathbf{E} \tag{4}$$

$$\mathbf{F}_c = k_c \frac{q'q}{|\mathbf{r} - \mathbf{r}'|^3}(\mathbf{r} - \mathbf{r}') \tag{5}$$

Equation (3) is Stoke's drag equation, suitable for low Reynolds number systems such as ours. It is notably a function of the radius, R, of the MP's bob, and of the bob's velocity, $\mathbf{v}$. Equation (4) is the Lorentz force, described by the vertically directed electric field, E, in our domain. Equation (5) is the Coulomb force, where $\mathbf{r} - \mathbf{r}'$ denotes the spatial vector directed from the MP of interest to a neighbouring MP, and k_c is Coulomb's constant. Equation (3) can be rewritten using the Stokes–Einstein relation to show the explicit dependence of drag on the diffusion coefficient of the bob as follows:

$$\mathbf{F}_d = \frac{k_B T}{D}\mathbf{v} \tag{6}$$

Next, the system is formalized using θ as the generalized coordinate with the bob constrained to always be one linker length, l, from its pivot. This required the following basic transformation and associated position derivatives:

$$\begin{cases} x = l\sin\theta \\ y = l\cos\theta \end{cases} \tag{7}$$

The EOMs are first solved in cartesian coordinates as a system of equations:

$$\begin{cases} m\ddot{x} = F_d^x + F_c^x \\ m\ddot{y} = F_d^y + F_c^y + F_e^y \end{cases} \tag{8}$$

Equation (8) is used to solve for the EOM of a single MP relative to its two neighbouring MPs. To use our MP model in a monolayer simulation, we must solve for three MPs, that is, the n, $n-1$ and $n+1$ MP, in a domain with periodic boundaries. Each MP is a distance d apart. Solving the system of equations from equation (8) and utilizing transformations from equation (7) for the set of three generalized MPs, we obtain the EOMs for our system:

$$\begin{cases} ml\ddot{\theta}_n = \frac{kq_nq_{n+1}(l\sin(\theta_n-\theta_{n+1})-d\cos\theta_n)}{[2l^2+d^2+2dl(\sin\theta_{n+1}-\sin\theta_n)-2l^2\cos(\theta_{n+1}-\theta_n)]^{\frac{3}{2}}} \\ \quad + \frac{kq_nq_{n-1}(l\sin(\theta_n-\theta_{n-1})+d\cos\theta_n)}{[2l^2+d^2-2dl(\sin\theta_{n-1}-\sin\theta_n)-2l^2\cos(\theta_{n-1}-\theta_n)]^{\frac{3}{2}}} \\ \quad -6\pi\eta Rl\dot{\theta}_n - q_nE_y\sin\theta_n \\ ml\ddot{\theta}_{n+1} = \frac{kq_{n+1}q_{n-1}(l\sin(\theta_{n+1}-\theta_{n-1})-d\cos\theta_{n+1})}{[2l^2+d^2+2dl(\sin\theta_{n-1}-\sin\theta_{n+1})-2l^2\cos(\theta_{n-1}-\theta_{n+1})]^{\frac{3}{2}}} \\ \quad + \frac{kq_{n+1}q_n(l\sin(\theta_{n+1}-\theta_n)+d\cos\theta_{n+1})}{[2l^2+d^2-2dl(\sin\theta_n-\sin\theta_{n+1})-2l^2\cos(\theta_n-\theta_{n+1})]^{\frac{3}{2}}} \\ \quad -6\pi\eta Rl\dot{\theta}_{n+1} - q_{n+1}E_y\sin\theta_{n+1} \\ ml\ddot{\theta}_{n-1} = \frac{kq_{n-1}q_n(l\sin(\theta_{n-1}-\theta_n)-d\cos\theta_{n-1})}{[2l^2+d^2+2dl(\sin\theta_n-\sin\theta_{n-1})-2l^2\cos(\theta_{n+1}-\theta_{n-1})]^{\frac{3}{2}}} \\ \quad + \frac{kq_{n-1}q_{n+1}(l\sin(\theta_{n-1}-\theta_{n+1})+d\cos\theta_{n-1})}{[2l^2+d^2-2dl(\sin\theta_{n+1}-\sin\theta_{n-1})-2l^2\cos(\theta_{n+1}-\theta_{n-1})]^{\frac{3}{2}}} \\ \quad -6\pi\eta Rl\dot{\theta}_{n-1} - q_{n-1}E_y\sin\theta_{n-1} \end{cases} \tag{9}$$

Equation (9) is the generalized description of the MP monolayer considering Coulomb force, Stoke's drag force and Lorentz force. This equation serves as a template for MP dynamics and can be modified with additional forces as needed. In our case, the first two terms are involved with the MP's electrostatic interactions with neighbouring strands, which push or pull MPs away from each other, the third term is the drag term resisting the rotational motion of the MP with different-sized analytes, and the final term is the force due to the charged bob's drift in an electric field. We solve the system of equations by transforming each equation into two first-order differential equations using the following relationship for angular velocity:

$$\omega = \dot{\theta} \tag{10}$$

With equation (10), each equation in the system described by equation (9) can be evaluated as an ordinary differential equation (ODE) for $\dot{\omega}(\theta)$ and $\dot{\theta}(\theta)$ using any ODE numerical solver. We opted to use a fourth-order Runge–Kutta, which we coded using MATLAB.

The EOMs are solved in picosecond resolution. Initial conditions of zero initial velocity and various starting angles are used. The EOMs are solved for each time step and the simulation is halted once the nth strand's bob hits the electrode surface (that is, $y = 0$). Only the information from the nth strand is needed for downstream analysis.

In a realized MP biosensor, a redox reporting molecule was attached at the distal end of the MP, meaning that as one MP transits to the electrode surface, a one-electron tunnelling current will be produced. To simulate a realistic situation, we used a DNA linker as the pendulum arm, antibody as the bob, and modulated the bob with bound protein analytes. In general, our MPs were computationally devised as a 24 mer dsDNA pendulum arm, with the bob of the unbound sensor as an immunoglobulin-G (IgG)-formatted antibody, which we estimate to be ~10 nm in diameter and 150 kDa. We estimated the corresponding analyte size by averaging the short- and long-axis protein lengths using database information from UniProt, roughly estimated its charge contribution by observing its pI from PhosphoSite and roughly took the charge magnitude as the difference from neutral pH. We also considered the charged species being shielded by the electrolyte, so we approximated the bob charge to be scaled down by the medium permittivity[49].

To gain confidence in our model being accurately determined, we performed a first-order approximation to determine the characteristic time of the MP EOMs. By simply considering the bob falling straight down to the surface in a time-averaged electric field with negligible Coulomb interactions with other bobs, we can analytically solve for the velocity of the EOMs. From here we can approximate the characteristic time of the model as

$$\tau = A_0 \frac{6\pi\eta\epsilon_r lR}{|q|E_{avg}} = A_0 \frac{\epsilon_r l k_B T}{|q|E_{avg} D} \tag{11}$$

Here, we have solved for the characteristic time assuming a positive applied electrode potential and net negatively charged DNA/recognition element/analyte. We see that, as the pendulum arm length increases, the time to fall, or characteristic time (τ) of the bob, increases because the transit time of the linker is longer. Similarly, as the analyte radius increases, or in other words the diffusion coefficient of the analyte decreases, τ increases as the bob experiences more drag as it moves in the electric field. As the negative charge of the analyte increases

(note that the charge is always a negative value for a DNA linker), τ decreases as the bob is pulled down faster towards the positive electrode surface. We also note that the viscosity and medium permittivity linearly modulate the τ of the system, which aids in predicting our system dynamics in different biofluids. Note how mass does not appear in the approximation—this is because the contribution of mass is quite negligible for our microscale system. However, as the mass and size generally increase together for realistic biomolecules, we still consider mass an important metric. We include a constant A_0 term in equation (11) to let the reader know that the equation is an approximation to determine the relative changes in parameters, whereas the fully realized equation (9) should be used for more accurate predictions.

The characteristic time of the system—whether it be determined by using equation (11) or by solving equation (9) for the average τ over MPs with random starting angles—can be used as a prediction of the electron-transfer decay rate of the system. What this means is that our MP system provides a dynamic readout of how the system reacts in the presence of bound analytes, in contrast to conventional electrochemical readouts, which rely on steady-state characterization. The τ of our system can be considered the characteristic time of a linear time-invariant system, meaning the electron-transfer output, as a current measurement, has the following form:

$$I(t) = I_0 e^{-\frac{t}{\tau}} = I_0 e^{-k_{\text{eff}} t} \tag{12}$$

Here, $k_{\text{eff}} = \frac{1}{\tau}$ is the effective electron-transfer rate.

More rigorously, we can numerically solve for a monolayer of MPs for a given probe density by iteratively solving for the MP τ over randomly sampled starting angles. The current is then calculated from τ data by generating a histogram, such that each bin holds the number of electron-transfer events for the binned time interval.

To compare the change in electron-transfer dynamics between bound and unbound MPs, we can take the ratio $k_{\text{eff bound}}$:$k_{\text{eff unbound}}$. The values for k_{eff} can be determined from the theoretical model by finding the average τ of protein analytes over randomly sampled initial angles. The k_{eff} from experimental data can be found by making a simple exponential fit to the decay portion of chronoamperometric data or by taking the reciprocal of the time at which the peak current has fallen to 1/e (36.8%) of its magnitude (the characteristic time for linear time-invariant systems).

Materials. The linker sequences are 5′-SH-MC6-TAC CAG CTA TTG TAT CTA ATA AGA-NH_2-3′ (24 mer P1), 5′-NH_2-C6-TCT TAT TAG ATA CAA TAG CTG GTA (24 mer P2), 5′-SH-MC6-TAC CAG CTA TTG TAT CTA ATA AGA TTT TTT TTT TTT TTT TTT TTT TTT-NH_2-3′ (48 mer P1), 5′-NH_2-C6-AAA AAA AAA AAA AAA AAA AAA AAA TCT TAT TAG ATA CAA TAG CTG GTA (48 mer P2), 5′-SH-MC6-TAC CAG CTA TTG TAT CTA ATA AGA TTT TTT TTT T-NH_2-3′ (34 mer P1), 5′-SH-MC6-TAC CAG CTA TTG TAT-NH_2-3′ (15 mer P1). All of the DNA sequences were obtained from Integrated DNA Technologies (IDT). Ferrocene-NHS ester was obtained from Five Photon Biochemicals. All of the antibodies and proteins were obtained from AbCam and R&D Systems. Recombinant human cardiac troponin I protein (CTI, ab207624), anti-CTI antibody (ab10321, mouse monoclonal, clone number 4C2, and isotype IgG2a), recombinant human cardiac troponin T protein (CTT, ab86685), anti-CTT antibody (ab8295, mouse monoclonal, clone number 1C11, and isotype IgG1), natural human IgE protein (ab152001), anti-IgE antibody (ab195580, rabbit monoclonal, clone number RM122, and isotype IgG, recombinant human brain natriuretic peptide (BNP) protein (ab87200), anti-BNP antibody (ab239510, mouse monoclonal, clone number C10, and isotype IgG2b), recombinant human/murine/rat brain-derived neurotrophic factor (BDNF) protein (ab9794), recombinant anti-BDNF antibody (ab108319, rabbit monoclonal, clone number EPR1292, and isotype IgG), recombinant human p53 protein (ab43615), anti-p53 antibody (ab26, mouse monoclonal, clone number PAb 240, and isotype IgG1), recombinant human alpha 1 fetoprotein (AFP, ab114216), anti-AFP antibody (ab3980, mouse monoclonal, clone number AFP-01, and isotype IgG1), recombinant human carcino embryonic antigen (CEA) protein (ab158095), anti-CEA antibody (ab4451, mouse monoclonal, clone number 26/3/13, and isotype IgG1), recombinant human thioredoxin (TRX) protein (ab51064), anti-TRX antibody (ab16965, mouse monoclonal, clone number 3A1, and isotype IgG2b), recombinant human IL-8 protein (ab9631) and anti-IL-8 antibody (ab18672, mouse monoclonal, clone number 807, and isotype IgG1) were obtained from AbCam. Recombinant human CCL5/RANTES protein (278-RN), human CCL5/RANTES anti-rantes antibody (MAB278, monoclonal mouse IgG1 and clone number 21445), recombinant human IL-6 protein (7270-IL) and anti-IL-6 antibody (MAB2061, mouse monoclonal, clone number 1936, and isotype IgG2B) were obtained from R&D Systems. $HAuCl_4$ solution, doxorubicin hydrochloride, tris(2-carboxyethyl)phosphine hydrochloride (TCEP) and 6-mercapto-1-hexanol (MCH) were obtained from Sigma-Aldrich. Sterile PBS and UltraPure DNase/RNase-free distilled water were obtained from Wisent Bioproducts. Saliva, tear, urine and sweat were obtained from Lee Biosolutions. Human blood and urine were collected from healthy volunteers.

Ferrocene conjugation. Ferrocene was conjugated to the amine-terminated DNA sequences by following the protocol supplied by the company (Five Photon Biochemicals). Briefly, ferrocene-NHS ester (9.85 mg, 30.11 µmol) was dissolved in 1.0 ml of methyl sulfoxide and 3 µmol amino-oligonucleotide was dissolved in 800 µl of 0.2 M sodium carbonate buffer (pH 8.5). The ester solution (400 µl) was added to the amino-oligonucleotide solution. The mixture was incubated for 4 h at room temperature or 16 h at 4 °C, after which it was purified by using chromatography on a Sephadex G-25 column using de-ionized (DI) water/carbonate buffer (50/50) as eluent. The fraction with yellow colour was dialyzed against water to remove excess salts and unreacted reagents.

Antibody conjugation. Antibody was conjugated to the amine-terminated DNA sequences by using antibody–oligonucleotide conjugation kits obtained from Solulink (Version 12.12.2012) and Abcam (ab218260, version 2). The antibody conjugation product was used for all experiments, where the protocol dilutes the stock antibody (1 mg ml^{-1}) five times.

Sensor fabrication. Fabrication of the chips and growth of the nanostructured sensors were performed as described previously, with little modification[50]. Briefly, glass chips were fabricated in house utilizing substrates obtained from Evaporate Metal Films; these were pre-coated with 5 nm Cr/100 nm Au. S1811 positive photoresist (MicroChem) was spin-coated onto the substrates in house (4,500 r.p.m., 90 s). Sensing electrodes were patterned using standard photolithography and etched using Au and Cr wet etchants followed by removal of the positive photoresist etchant mask. We spin-coated a negative photoresist SU-8 2002 (3,000 r.p.m., 60 s) to create 20-µm apertures. After cleaning the chips with acetone, isopropyl alcohol and DI water, sensors were electroplated in apertures in a solution of 50 mM $HAuCl_4$ and 0.5 M HCl using d.c. potential amperometry at 0 mV for 100 s. A fine nanostructured Au coating was formed on the Au structure during a second electrodeposition step in the same solution of Au at −450 mV for 10 s (ref. [38]).

Sensor functionalization. A 1 µM thiolated probe solution in PBS was mixed with 1 mM TCEP for disulfide reduction and incubated for an hour in a dark chamber. This thiolated probe (P1) contained a thiol group at the 5′ end and ferrocene redox reporter at the other end. The probe solution was heated to 55 °C for 5 min and chilled, then 1 µM antibody-conjugated complementary probe (P2) was mixed into the thiolated probe mixture and incubated for 10 min to hybridize. MCH solution (9 µM) was mixed into the probe mixtures. The probe solution was then dropped onto the chips and incubated overnight in a dark humidity chamber at room temperature for immobilization of the probe. The chip was washed twice for 5 min with 1× PBS at room temperature and once more with 0.1× PBS. Before the experiment, sensors were kept immersed in 0.1× PBS solution. After initial electrochemical scanning, the chips were treated with different targets at room temperature for 50 min. After target incubation, chronoamperometric experiments were performed in the same solution without washing the sensor.

Animal study. All animal experiments were conducted according to a protocol approved by the University of Toronto Animal Care Committee, which follows the guidelines and standards of the Canadian Council on Animal Care (CCAC). Six- to eight-week-old C57BL/6J male mice (Jackson Laboratory) were used in all studies. To induce acute cardiotoxicity, mice were injected intraperitoneally with doxorubicin (10 mg kg^{-1}) for four days. At day 5, saliva samples were collected or in situ measurements were carried out in control and treated mice. For the continuous monitoring experiments, we administered troponin I (50 µg per mouse) via tail vein injection and measured the signal with electrodes placed in the oral cavity of the mice. Saliva samples at different time points were also collected for in vitro analysis.

Electrochemical analysis. Electrochemical experiments were carried out using a BASi Epsilon-EC (version 2.00.71_USB software) potentiostat with a three-electrode system featuring the sensor as the working electrode, Ag/AgCl (or on-chip gold) as the reference electrode and a platinum wire (or on-chip gold) as the counter electrode. Electrochemical signals were recorded using chronoamperometry using a potential window from 0 to +500 mV (versus Ag/AgCl) or −200 to +300 mV (versus the pseudo gold reference electrode) for 50 ms. Each measurement that was performed for a single condition (that is, one antibody, one protein and one biofluid) was taken on a minimum of three working electrodes to produce replicates. Data were analysed using MATLAB R2018a and SigmaPlot 10.0.

Determination of probe density. For measuring the probe surface density, chronocoulometry was performed in 0.1× PBS in the presence and absence of 100 µM $[Ru(NH_3)_6]_{3+}$ after purging it thoroughly with nitrogen gas with a pulse period of 250 ms and a pulse width of 0.7 V (from +0.20 to −0.50 V). Following the published protocol, the calculated surface density of the double-stranded DNA probe was $(1.5 \pm 0.38) \times 10^{12}$ molecules cm^{-2}, or 1 probe per 66 nm^2. The surface area of the sensors $(3.5 \pm 0.25) \times 10^{-4}$ cm^2 was calculated by integrating the Au oxide reduction peak area obtained from a cyclic voltammogram in 100 mM H_2SO_4. The surface area was calculated by integrating the reduction peak to obtain the reduction charge and dividing this by 386 µC cm^{-2} (ref. [51]).

Reporting Summary. Further information on research design is available in the Nature Research Reporting Summary linked to this Article.

Data availability

The main data supporting the findings of the current study are available within the paper and its Supplementary Information. Data for figures in the Supplementary Information are included as additional Supplementary files. Data for chemical and physical protein parameters were derived from UniProt (https://www.uniprot.org/) and PhosphoSitePlus (https://www.phosphosite.org/). Source data are provided with this paper.

Code availability

The code corresponding to the theoretical model for the MP can be accessed at https://github.com/sgomis/MP-biosensor.

References

48. Bard, A. & Faulkner, L. *Electrochemical Methods*: *Fundamentals and Applications* 2nd edn (John Wiley & Sons, 1944).
49. Maffeo, C. et al. Close encounters with DNA. *J. Phys. Condens. Matter* **26**, 413101 (2014).
50. Lam, B. et al. Optimized templates for bottom-up growth of high-performance integrated biomolecular detectors. *Lab Chip* **13**, 2569–2575 (2013).
51. Rand, D. A. J. & Woods, R. The nature of adsorbed oxygen on rhodium, palladium and gold electrodes. *J. Electroanal. Chem.* **31**, 29–38 (1971).

Acknowledgements

This research is supported by the Canadian Institutes of Health Research (FDN-148415, CHRPJ 523597-18) and the Natural Sciences and Engineering Research Council of Canada (2016-06090, CHRPJ 523597-18). Assets from BioRender.com were used in the main text figures. All correspondence and requests for materials should be made to S.O.K.

Author contributions

J.D., S.G., E.H.S. and S.O.K. conceived the experiments. J.D. and S.G. designed and performed the experiments. S.G. conceived the theoretical model. J.B.C. fabricated the chips. J.D. and A.M. fabricated electrodes. H.Y. and W.Z. performed conjugation of ferrocence to oligo and antibody to oligo. S.A., J.D. and S.G. performed experiments with the animal model and J.D., S.G., E.H.S. and S.O.K. co-wrote the manuscript.

Competing interests

The authors declare no competing interests.

Additional information

Supplementary information The online version contains supplementary material available at https://doi.org/10.1038/s41557-021-00644-y.

Correspondence and requests for materials should be addressed to E.H.S. or S.O.K.

Peer review information *Nature Chemistry* thanks Netz Arroyo and the other, anonymous, reviewer(s) for their contribution to the peer review of this work.

Reprints and permissions information is available at www.nature.com/reprints.

nature research

Corresponding author(s): Shana Kelley

Last updated by author(s): Dec 21, 2020

Reporting Summary

Nature Research wishes to improve the reproducibility of the work that we publish. This form provides structure for consistency and transparency in reporting. For further information on Nature Research policies, see our Editorial Policies and the Editorial Policy Checklist.

Statistics

For all statistical analyses, confirm that the following items are present in the figure legend, table legend, main text, or Methods section.

n/a	Confirmed	
☐	☒	The exact sample size (*n*) for each experimental group/condition, given as a discrete number and unit of measurement
☐	☒	A statement on whether measurements were taken from distinct samples or whether the same sample was measured repeatedly
☐	☒	The statistical test(s) used AND whether they are one- or two-sided *Only common tests should be described solely by name; describe more complex techniques in the Methods section.*
☒	☐	A description of all covariates tested
☒	☐	A description of any assumptions or corrections, such as tests of normality and adjustment for multiple comparisons
☐	☒	A full description of the statistical parameters including central tendency (e.g. means) or other basic estimates (e.g. regression coefficient) AND variation (e.g. standard deviation) or associated estimates of uncertainty (e.g. confidence intervals)
☐	☒	For null hypothesis testing, the test statistic (e.g. *F*, *t*, *r*) with confidence intervals, effect sizes, degrees of freedom and *P* value noted *Give P values as exact values whenever suitable.*
☒	☐	For Bayesian analysis, information on the choice of priors and Markov chain Monte Carlo settings
☒	☐	For hierarchical and complex designs, identification of the appropriate level for tests and full reporting of outcomes
☒	☐	Estimates of effect sizes (e.g. Cohen's *d*, Pearson's *r*), indicating how they were calculated

Our web collection on statistics for biologists contains articles on many of the points above.

Software and code

Policy information about availability of computer code

Data collection	BASi Epsilon-EC - Ver. 2.00.71_USB
Data analysis	Matlab R2018a, SigmaPlot 10.0

For manuscripts utilizing custom algorithms or software that are central to the research but not yet described in published literature, software must be made available to editors and reviewers. We strongly encourage code deposition in a community repository (e.g. GitHub). See the Nature Research guidelines for submitting code & software for further information.

Data

Policy information about availability of data

All manuscripts must include a data availability statement. This statement should provide the following information, where applicable:

- Accession codes, unique identifiers, or web links for publicly available datasets
- A list of figures that have associated raw data
- A description of any restrictions on data availability

The main data supporting the findings of the current study are available within the paper and its Supplementary Information. Source data for figures 1-4 are provided in the paper, and data for figures in the Supplementary Information are included as additional Supplementary files. Data for chemical and physical protein parameters were derived from UniProt (https://www.uniprot.org/) and PhosphoSitePlus (https://www.phosphosite.org/).

Field-specific reporting

Please select the one below that is the best fit for your research. If you are not sure, read the appropriate sections before making your selection.

☒ Life sciences ☐ Behavioural & social sciences ☐ Ecological, evolutionary & environmental sciences

For a reference copy of the document with all sections, see nature.com/documents/nr-reporting-summary-flat.pdf

Life sciences study design

All studies must disclose on these points even when the disclosure is negative.

Sample size	No sample-size calculations were performed, and samples sizes were arbitrarily chosen according to the conventions in the field. For a single experimental condition, e.g. detection of a single protein in a single bio-fluid, the number of replicates was at least 3 biological replicates (that is, independent experiments) and/or at least 3 technical replicates (that is, repeated measurements of the same original sample). Our sensor performance was validated using 10 different proteins and in 5 different biofluids, and negative controls in our investigation including no target, non-target proteins, and BSA targets - a minimum triplicate was deemed sufficient as all variables change just two outcomes - unbound and bound signal.
Data exclusions	Few data were excluded in cases where there was instrument or human error, such as there being no electrochemical signal due to mechanical connection issues or damage to the sensors due to physical scratching. Exclusions occurred for when the metal pin connections to the sensor would not be pressed tightly against the sensor pads, when the soldered ends of the clamps that connect the sensors to the measurement device would break, or in mouse study trials where teeth would scratch the active electrode area of the sensor and cause the measured signal to disappear.
Replication	At least three individual measurements were performed for each experimental condition to replicate the data. All replicates were successful, except for cases requiring data exclusion as mentioned above.
Randomization	Data was obtained with different concentrations of target proteins and also tested with control sensors and negative target proteins. Randomization is not relevant to the study as the experimental conditions are based on antibodies and proteins provided from homogeneous batches.
Blinding	No blinded experiments were performed. Blinding was not relevant to the study as we were exploring the range of applications of our sensor and not using out sensor to provide clinical results.

Reporting for specific materials, systems and methods

We require information from authors about some types of materials, experimental systems and methods used in many studies. Here, indicate whether each material, system or method listed is relevant to your study. If you are not sure if a list item applies to your research, read the appropriate section before selecting a response.

Materials & experimental systems

n/a	Involved in the study
☐	☒ Antibodies
☒	☐ Eukaryotic cell lines
☒	☐ Palaeontology and archaeology
☐	☒ Animals and other organisms
☐	☒ Human research participants
☒	☐ Clinical data
☒	☐ Dual use research of concern

Methods

n/a	Involved in the study
☒	☐ ChIP-seq
☒	☐ Flow cytometry
☒	☐ MRI-based neuroimaging

Antibodies

Antibodies used	Dilutions and conditions of use are provided in the Methods section. -Anti-cardiac troponin I (CTI) antibody (ab10321, mouse monoclonal, clone number 4C2, isotype IgG2a, RRID:AB_296967, multiple lots) -Anti-cardiac troponin T (CTT) antibody (ab8295, mouse monoclonal, clone number 1C11, isotype IgG1, RRID:AB_306445, multiple lots) -Anti-IgE antibody (ab195580, rabbit monoclonal, clone number RM122, isotype IgG, multiple lots) -Anti-brain natriuretic peptide (BNP) antibody (ab239510, mouse monoclonal, clone number C10, isotype IgG2b, multiple lots) -Recombinant anti-human/murine/rat brain-derived neurotrophic factor (BDNF) antibody (ab108319, rabbit monoclonal, clone -number EPR1292, isotype IgG, RRID:AB_10862052, multiple lots) -Anti-p53 antibody (ab26, mouse monoclonal, clone number PAb 240, isotype IgG1, RRID:AB_303198, multiple lots) -Anti-alpha 1 fetoprotein (AFP) antibody (ab3980, mouse monoclonal, clone number AFP-01, isotype IgG1, RRID:AB_304203, multiple lots)

-Anti-carcino embryonic antigen (CEA) antibody (ab4451, mouse monoclonal, clone number 26/3/13, isotype IgG1, RRID:AB_304463, multiple lots)
-Anti-human thioredoxin (TRX) antibody (ab16965, mouse monoclonal, clone number 3A1, isotype IgG2b, RRID:AB_443587, multiple lots)
-Anti-IL-8 antibody (ab18672, mouse monoclonal, clone number 807, isotype IgG1, RRID:AB_444617, multiple lots)
-Anti-CCL5/RANTES antibody (MAB278, monoclonal mouse IgG1, clone number 21445, RRID:AB_358196, multiple lots)
-Anti-IL-6 antibody (MAB2061, mouse monoclonal, clone number 1936, isotype IgG2B, RRID:AB_2127616, multiple lots)

Validation

All antibodies utilized in this study were validated by the manufacturers and validation data are available online at the manufacturers' websites. The antibodies were validated by flow cytometry and/or Western blotting and/or immunocytochemistry and/or immunohistochemistry. Details about the used antibodies and the suppliers are provided in the previous section.

Animals and other organisms

Policy information about studies involving animals; ARRIVE guidelines recommended for reporting animal research

Laboratory animals	6 to 8 weeks old C57BL/6J male mice (Jackson Laboratory) were used in all studies and maintained under standard housing conditions regulated by the University of Toronto animal facility.
Wild animals	The study did not involve wild animals.
Field-collected samples	The study did not include field-collected samples.
Ethics oversight	All animal experiments were conducted according to the protocol approved by the University of Toronto Animal Care Committee, which follows the guidelines and standards of Canadian Council on Animal Care (CCAC).

Note that full information on the approval of the study protocol must also be provided in the manuscript.

Human research participants

Policy information about studies involving human research participants

Population characteristics	Health volunteers (male and female, aged 20-40) were recruited from the University of Toronto for urine and blood samples to be used for in vitro sensing experiments.
Recruitment	All patients were enrolled subsequent to informed consent with no self-selection bias.
Ethics oversight	Required consent from the participants and approval from the institutional biosafety committee of University of Toronto was taken prior to use of human body fluids in all experiments related to this project.

Note that full information on the approval of the study protocol must also be provided in the manuscript.